

High-fidelity and controllable cloning of high-dimensional optical beams with a Rydberg atomic gas

Lu Qin,¹ Chao Hang,^{1,2} and Guoxiang Huang^{1,2,3}

¹*State Key Laboratory of Precision Spectroscopy, East China Normal University, Shanghai 200062, China*

²*NYU-ECNU Joint Institute of Physics, New York University Shanghai, Shanghai 200062, China*

³*Collaborative Innovation Center of Extreme Optics, Shanxi University, Taiyuan, Shanxi 030006, China*



(Received 2 June 2020; accepted 23 November 2020; published 9 December 2020)

High-fidelity and controllable optical cloning of high-dimensional (high-D) optical beams is very important for the development of novel techniques for optical imaging, lithography, and communications, etc. Here we propose a scheme to realize the cloning of high-D optical beams with a Rydberg atomic gas via electromagnetically induced transparency. We show that strong atom-atom interaction can map to two probe laser fields, which may acquire giant nonlocal Kerr nonlinearities supporting the formation of stable high-D optical solitons and vortices at very low light power. We also show that such optical solitons and vortices prepared in one probe field can be cloned onto another one with high fidelity, and the cloning may be actively manipulated through the tuning of the nonlocality degree of the Kerr nonlinearities. Moreover, we demonstrate that based on such a cloning scheme multitudes and multicomponents cloning of high-D optical beams are also possible, which allows us to acquire multiple copies of high-D optical beams. The results on the optical cloning reported here are not only of fundamental interest for nonlocal nonlinear optics but also promising for practical applications in optical information processing and transmission.

DOI: [10.1103/PhysRevA.102.063707](https://doi.org/10.1103/PhysRevA.102.063707)

I. INTRODUCTION

Due to practical applications in optical imaging, switching, lithography, and free-space communication technologies, great efforts have been paid to the investigation on optical guiding, steering, and cloning. However, transmitted images with finite size imprinted in an optical beam are usually distorted significantly because of diffraction effect even after propagating only a few Rayleigh lengths, which leads to a fundamental limitation to the transmission of small optical images [1,2].

To suppress diffraction, in the past two decades many schemes have been proposed based on various atomic coherence effects, including electromagnetically induced transparency (EIT) [3–10], coherent population trapping [11–18], saturated absorption [19], active Raman gain [20], electromagnetically induced absorption [21], and so on. The physical mechanism behind these schemes can be understood through the induced space-dependent refractive index contributed by a strong, spatially modulated control field, which results in self-focusing (waveguiding [5,6,22,23]) or self-defocusing (antiwaveguiding [24]) for the propagation of a weak probe field, and thereby an arbitrary optical image carried by the control field can be converted or cloned onto a probe field.

The cloning of optical images beyond diffraction in atomic gases, however, remains to be a challenging task due to the following reasons. First, most of the schemes mentioned above have low transmission due to the presence of optical absorption. Even for the atomic gas working with conventional EIT schemes, the space-modulated control field used for cloning is not stronger than the probe field in some spatial regions, where

the EIT condition is violated. Second, in the region where the control field is weak, the propagation of the probe field results in a pronounced change of the control field, and hence the images imprinted in the control field might be distorted before and after they are cloned onto the probe field. Third, in free space the diffraction effect for small images is not negligible and the quality of the optical cloning is lowered significantly.

In this paper, we propose a scheme to realize the cloning of high-dimensional (high-D) optical beams. Here high-D optical beams mean $(2 + 1)$ D optical ones, with “2” denoting two transverse coordinates (e.g., x and y) and “1” denoting the longitudinal coordinate (e.g., propagation coordinate z); see below. The system we adopted is a cold Rydberg atomic gas [25,26] with an inverted Y-type level configuration, coupled with two weak probe laser fields and a control laser field with no space modulation. Based on the mechanism of a double Rydberg-EIT [27], we show that the strong, nonlocal atom-atom interaction (also called Rydberg-Rydberg interaction) can map to the two probe laser fields, which may acquire giant, nonlocal self-Kerr and cross-Kerr nonlinearities that can suppress diffraction and hence stabilize high-D optical solitons and vortices of very low light power. We also show that by virtue of the cross-Kerr nonlinearities such high-D optical solitons and vortices prepared in one probe field can be cloned onto another probe field with high fidelity of waveshape; furthermore, the cloning can be actively controlled through the manipulation of the nonlocality degree of the Kerr nonlinearities. In addition, we demonstrate that it is possible to realize multitudes and multicomponents cloning of high-D optical beams, which allows us to acquire multiple copies through such a cloning scheme. The findings for optical cloning

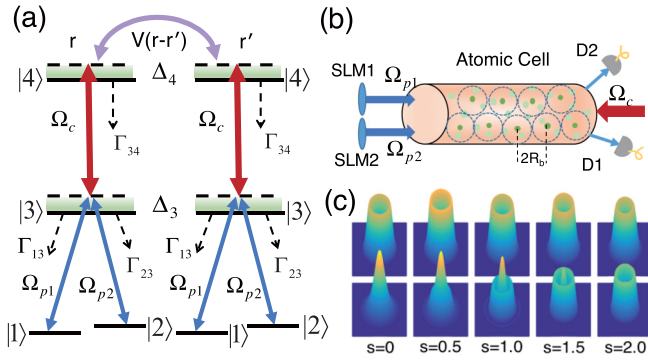


FIG. 1. Schematics of the model. (a) Inverted Y-type level diagram and excitation scheme of the double Rydberg-EIT. The weak probe laser field with half Rabi frequency Ω_{p1} (Ω_{p2}) couples the transition $|1\rangle \leftrightarrow |3\rangle$ ($|2\rangle \leftrightarrow |3\rangle$); the strong control laser field with half Rabi frequency Ω_c couples the transition $|3\rangle \leftrightarrow |4\rangle$, with $|4\rangle$ a Rydberg state; Δ_α are detunings and $\Gamma_{\alpha\beta}$ are spontaneous emission decay rates; $V_{\text{vdw}} = \hbar V(\mathbf{r}' - \mathbf{r})$ is the van der Waals interaction potential between the two Rydberg atoms located at \mathbf{r}' and \mathbf{r} , respectively. (b) The long-range interaction between Rydberg atoms blocks the excitation of the atoms within blockade spheres [the blockade spheres boundary indicated by the blue dashed lines] of radius R_b . In each blocked sphere only one Rydberg atom (small dark green sphere) is excited and other atoms (small light blue spheres) are prevented from being excited. The blue and red arrows indicate the propagating direction of the probe and control fields. SLM, space light modulator; D, detector. (c) Cloning of the optical vortex. The probe field 1 prepared to be an optical vortex (upper row) is cloned onto the probe beam 2 (which is initially prepared to be a hyperbolic secant mode; lower row). Illustrated here are normalized peak intensity distributions of the both probe fields as functions of nondimensional propagation distance $s = z/(2L_{\text{diff}})$ (L_{diff} is typical diffraction length).

reported here are not only of fundamental interest for the development of nonlocal nonlinear optics based on Rydberg atomic gases [28–32], but also useful for high-fidelity and controllable optical cloning and hence promising for applications in information processing and transmission, including diffractionless biological and medical imaging [33,34].

The paper is arranged as follows. In Sec. II, we present the physical model and derive coupled nonlinear equations that describe the propagation of the two probe laser fields by using a method of multiple scales beyond mean-field approximation. In Sec. III, we investigate how to clone high-D nonlocal optical solitons and vortices from one probe field onto another one. In Sec. IV, we extend our investigation to the realization of the multitudes and multicomponents cloning of high-D optical beams. Finally, Sec. V gives a summary of the main results obtained in this paper.

II. MODEL AND COUPLED NONLINEAR EQUATIONS

A. Physical model

We start with considering a cold gas of Rydberg atoms with an inverted Y-type four-level configuration [see Fig. 1(a)], where two weak probe laser fields with center frequencies ω_{p1} and ω_{p2} (half Rabi frequencies Ω_{p1} and Ω_{p2}) couple the

transitions $|1\rangle \leftrightarrow |3\rangle$ and $|2\rangle \leftrightarrow |3\rangle$, respectively; a strong control laser field with center frequency ω_c (half Rabi frequency Ω_c) couples the transition $|3\rangle \leftrightarrow |4\rangle$, where $|4\rangle$ is a high-lying Rydberg state; Δ_α ($\alpha = 2, 3, 4$) are detunings; $\Gamma_{\alpha\beta}$ are spontaneous emission decay rates from $|\beta\rangle$ to $|\alpha\rangle$. The interaction between two Rydberg atoms, respectively, at positions \mathbf{r} and \mathbf{r}' is described by van der Waals potential $V_{\text{vdw}} \equiv \hbar V(\mathbf{r}' - \mathbf{r})$. A possible experimental geometry is shown in Fig. 1(b). Due to the long-range Rydberg-Rydberg interaction, a blockade phenomenon (called Rydberg blockade) occurs, by which an atom that has been excited to the Rydberg state $|4\rangle$ will block the excitation of other atoms within a blockade sphere (which has radius R_b). The role played by the Rydberg blockade makes the effective interaction between atoms (and also photons) finite. Note that in the inverted Y-shaped excitation scheme shown in Fig. 1(a) there are two ladder-type excitation paths, i.e., $|1\rangle \rightarrow |3\rangle \rightarrow |4\rangle$ and $|2\rangle \rightarrow |3\rangle \rightarrow |4\rangle$, which constitute two standard Rydberg-EITs (with the state $|4\rangle$ a shared Rydberg state). Thus the dynamics of the light fields and the atoms in the system can be taken to be controlled by a double Rydberg-EIT.

The electric field in the system reads $\mathbf{E} = \sum_{l=p1,p2,c} \mathbf{e}_l \mathcal{E}_l e^{i\theta_l(\mathbf{r},t)} + \text{c.c.}$. Here c.c. represents complex conjugate; $\theta_l(\mathbf{r}, t) = \mathbf{k}_l \cdot \mathbf{r} - \omega_l t$, with \mathbf{e}_l , \mathcal{E}_l , \mathbf{k}_l , and ω_l the unit polarization vector, envelope, wave vector, and angular frequency of the l th laser field, respectively. For simplicity and for suppressing Doppler effect, the two probe fields are assumed to propagate along the z direction (i.e., $\mathbf{k}_{pj} = k_{pj}\mathbf{e}_z$; $j = 1, 2$), while the control field propagates along the $-z$ direction (i.e., $\mathbf{k}_c = -k_c\mathbf{e}_z$), with \mathbf{e}_z the unit vector along the z direction.

Under electric dipole and rotating-wave approximations, the Hamiltonian of the system is $\hat{H} = \mathcal{N}_a \int d^3r \hat{\mathcal{H}}$; here $d^3r = dx dy dz$, \mathcal{N}_a is atomic density, and $\hat{\mathcal{H}}$ is the Hamiltonian density of the form

$$\begin{aligned} \hat{\mathcal{H}} = & - \sum_{\alpha=1}^4 \hbar \Delta_\alpha \hat{S}_{\alpha\alpha}(\mathbf{r}, t) - \hbar [\Omega_{p1} \hat{S}_{13}(\mathbf{r}, t) + \Omega_{p2} \hat{S}_{23}(\mathbf{r}, t) \\ & + \Omega_c \hat{S}_{34}(\mathbf{r}, t) + \text{H.c.}] \\ & + \mathcal{N}_a \int d^3r' \hat{S}_{44}(\mathbf{r}', t) \hbar V(\mathbf{r}' - \mathbf{r}) \hat{S}_{44}(\mathbf{r}, t), \end{aligned} \quad (1)$$

where $\hat{S}_{\alpha\beta} = |\beta\rangle\langle\alpha| \exp\{i[(\mathbf{k}_\beta - \mathbf{k}_\alpha) \cdot \mathbf{r} - (\omega_\beta - \omega_\alpha + \Delta_\beta - \Delta_\alpha)t]\}$ is the atomic transition operator related to the states $|\alpha\rangle$ and $|\beta\rangle$, satisfying the commutation relation $[\hat{S}_{\alpha\beta}(\mathbf{r}, t), \hat{S}_{\mu\nu}(\mathbf{r}', t)] = (1/\mathcal{N}_a)\delta(\mathbf{r} - \mathbf{r}') [\delta_{\alpha\nu}\hat{S}_{\mu\beta}(\mathbf{r}, t) - \delta_{\mu\beta}\hat{S}_{\alpha\nu}(\mathbf{r}, t)]$; $\Omega_{p1} = (\mathbf{e}_{p1} \cdot \mathbf{p}_{13})\mathcal{E}_{p1}/(2\hbar)$, $\Omega_{p2} = (\mathbf{e}_{p2} \cdot \mathbf{p}_{23})\mathcal{E}_{p2}/(2\hbar)$, and $\Omega_c = (\mathbf{e}_c \cdot \mathbf{p}_{34})\mathcal{E}_c/(2\hbar)$ are, respectively, half Rabi frequencies of the probe field 1, probe field 2, and control field, with $\mathbf{p}_{\alpha\beta}$ the electric dipole matrix element associated with the transition $|\beta\rangle \leftrightarrow |\alpha\rangle$; the detunings are given by $\Delta_1 = \Delta_2 = 0$, $\Delta_3 = \omega_{p1} - (E_3 - E_1)/\hbar$, and $\Delta_4 = \omega_c + \omega_{p1} - (E_4 - E_1)/\hbar$, with $E_\alpha = \hbar\omega_\alpha$ the eigenenergy of the state $|\alpha\rangle$. The last term on the right-hand side of Eq. (1) comes from the Rydberg-Rydberg interaction, described by the van der Waals potential $V_{\text{vdw}} = -\hbar C_6/|\mathbf{r}' - \mathbf{r}|^6$ (C_6 is called dispersion parameter [35]).

The dynamics of the atomic motion is controlled by the optical Bloch equation

$$\frac{\partial \hat{\rho}}{\partial t} = -\frac{i}{\hbar} [\hat{H}, \hat{\rho}] - \Gamma [\hat{\rho}], \quad (2)$$

where $\hat{\rho}$ is the density matrix (DM) describing the atomic population and coherence (with the DM elements defined by $\rho_{\alpha\beta} \equiv \langle \hat{S}_{\alpha\beta} \rangle$) and Γ is the relaxation matrix describing the spontaneous emission and dephasing. The explicit expression of Eq. (2) is presented in Appendix A.

The evolution of the probe field 1 and probe field 2 are controlled by the Maxwell equation $\nabla^2 \mathbf{E} - (1/c^2) \partial^2 \mathbf{E} / \partial t^2 = [1/(\epsilon_0 c^2)] \partial^2 \mathbf{P} / \partial t^2$, with $\mathbf{P} = \mathcal{N}_a \{ \rho_{13} \rho_{31} \exp[i(\mathbf{k}_{p1} \cdot \mathbf{r} - \omega_{p1} t)] + \rho_{23} \rho_{32} \exp[i(\mathbf{k}_{p2} \cdot \mathbf{r} - \omega_{p2} t)] + \text{c.c.} \}$. We assume that the two probe fields can be taken as classical fields and hence a semiclassical approach for the system can be adopted [36]. Under the paraxial and slowly varying envelope approximations, the Maxwell equation is reduced to [37]

$$i \left(\frac{\partial}{\partial z} + \frac{1}{c} \frac{\partial}{\partial t} \right) \Omega_{p1} + \frac{c}{2\omega_{p1}} \nabla_{\perp}^2 \Omega_{p1} + \kappa_{13} \rho_{31} = 0, \quad (3a)$$

$$i \left(\frac{\partial}{\partial z} + \frac{1}{c} \frac{\partial}{\partial t} \right) \Omega_{p2} + \frac{c}{2\omega_{p2}} \nabla_{\perp}^2 \Omega_{p2} + \kappa_{23} \rho_{32} = 0, \quad (3b)$$

$$i \frac{\partial}{\partial z} \Omega_{p1} + \frac{c}{2\omega_{p1}} \nabla_{\perp}^2 \Omega_{p1} + (W_{11} |\Omega_{p1}|^2 + W_{12} |\Omega_{p2}|^2) \Omega_{p1} + \int d^2 r'_{\perp} G_{11}(\mathbf{r}_{\perp} - \mathbf{r}'_{\perp}) |\Omega_{p1}(\mathbf{r}'_{\perp}, z)|^2 \Omega_{p1}(\mathbf{r}) + \int d^2 r'_{\perp} G_{12}(\mathbf{r}_{\perp} - \mathbf{r}'_{\perp}) |\Omega_{p2}(\mathbf{r}'_{\perp}, z)|^2 \Omega_{p1}(\mathbf{r}) = 0, \quad (4a)$$

$$i \frac{\partial}{\partial z} \Omega_{p2} + \frac{c}{2\omega_{p2}} \nabla_{\perp}^2 \Omega_{p2} + (W_{21} |\Omega_{p1}|^2 + W_{22} |\Omega_{p2}|^2) \Omega_{p2} + \int d^2 r'_{\perp} G_{21}(\mathbf{r}_{\perp} - \mathbf{r}'_{\perp}) |\Omega_{p1}(\mathbf{r}'_{\perp}, z)|^2 \Omega_{p2}(\mathbf{r}) + \int d^2 r'_{\perp} G_{22}(\mathbf{r}_{\perp} - \mathbf{r}'_{\perp}) |\Omega_{p2}(\mathbf{r}'_{\perp}, z)|^2 \Omega_{p2}(\mathbf{r}) = 0, \quad (4b)$$

with $\mathbf{r}_{\perp} = (x, y)$, $d^2 r'_{\perp} = dx' dy'$. Here the nonlinear coefficients W_{jj} ($j = 1, 2$) and W_{jl} ($j, l = 1, 2; j \neq l$) characterize, respectively, local self-Kerr and cross-Kerr nonlinearities (contributed by the weak, short-range interactions between photons and atoms, which are present for conventional double EIT systems [37]); G_{jj} and G_{jl} ($j \neq l$) are *nonlocal* nonlinear response functions characterizing, respectively, nonlocal self-Kerr and cross-Kerr nonlinearities (contributed by the strong, long-range Rydberg-Rydberg interaction). These nonlinear coefficients have the forms $W_{jl} = \kappa_{j3} a_{3j,l}^{(3)}$ and $G_{jl} = \kappa_{j3} \mathcal{N}_a \int dz V(\mathbf{r}' - \mathbf{r}) a_{3j,l+2}^{(3)}$, with explicit expressions of $a_{3j,l}^{(3)}$ and $a_{3j,l+2}^{(3)}$ given in Appendix B. Note that when obtaining Eq. (4) we have assumed that the spatial extension of the both probe fields in the z direction (order of centimeters) is much larger than that of the range of the Rydberg-Rydberg interaction (order of micrometers). It is worth indicating that due to the Rydberg blockade the interaction between photons is finite. This point is manifested clearly by the nonlocal nonlinear response functions G_{jl} , which approach a saturated value even when $\mathbf{r}' \rightarrow \mathbf{r}$; i.e., the effective interaction potential between photons is of a soft-core shape.

For the convenience of the following discussions and numerical calculations, we take a laser-cooled ^{87}Sr

where $\nabla_{\perp}^2 = \partial^2 / \partial x^2 + \partial^2 / \partial y^2$, $\kappa_{13} = \mathcal{N}_a \omega_{p1} |\mathbf{p}_{13}|^2 / (2\epsilon_0 c \hbar)$, and $\kappa_{23} = \mathcal{N}_a \omega_{p2} |\mathbf{p}_{23}|^2 / (2\epsilon_0 c \hbar)$, with ϵ_0 the vacuum dielectric constant.

B. Coupled nonlinear envelope equations

We are interested in the steady-state property of the system, for which the time derivative in the Maxwell-Bloch (MB) equations (2) and (3) can be neglected, valid for the two probe fields of long time durations. We expect that the initial population in the atomic states will not change significantly when the two nonlinear probe fields (which are weak compared with the control field) are applied to the system, and hence a perturbation expansion based on a method of multiple scales [38] can be used to solve the MB equations. However, due to the Rydberg-Rydberg interaction, atom-atom correlations should be taken into account suitably beyond mean-field approximation, which can be implemented by employing the technique developed recently in Refs. [39,40]. The detail of the calculation for solving the MB equations (2) and (3) based on such a perturbation expansion exact to third-order approximation is given in Appendix B, where it is shown that Ω_{p1} and Ω_{p2} obey the following (2 + 1)D coupled *nonlocal* nonlinear Schrödinger (CNNLS) equations:

atomic gas as a realistic, experimentally feasible example, for which the hyperfine atomic levels are assigned to be $|1\rangle = |5s^2 \ ^1S_0, F = 9/2, m_F = -1/2\rangle$, $|2\rangle = |5s^2 \ ^1S_0, F = 9/2, m_F = 3/2\rangle$, $|3\rangle = |5s 5p \ ^1P_1\rangle$, and $|4\rangle = |5s ns \ ^1S_0\rangle$. The dispersion parameter of the van der Waals potential for ^{87}Sr is $C_6 = 2\pi \times 10.9 \text{ GHz } \mu\text{m}^6$ for main quantum number $n = 50$, which can provide attractive Rydberg-Rydberg interaction [41–44], and hence the Kerr nonlinearities of the system will be self-focused ones [45]. The other system parameters are given by $\Gamma_3 \approx 2\pi \times 32 \text{ MHz}$, $\Gamma_4 \approx 2\pi \times 16.7 \text{ kHz}$; $\Delta_3 = -2\pi \times 240 \text{ MHz}$, $\Delta_4 = 2\pi \times 3 \text{ kHz}$, $\Omega_c = 2\pi \times 20 \text{ MHz}$. The choice of the large one-photon detuning Δ_3 is to make the system work in a dispersive regime of the double Rydberg-EIT, by which the spontaneous emission of the intermediate state $|3\rangle$ can be largely suppressed and hence the damping of the optical fields during propagation can be reduced greatly.

From Eqs. (4a) and (4b), one can obtain the expression of the optical susceptibility of the j th probe field, defined by $\chi_j = \mathcal{N}_a (\mathbf{e}_p \cdot \mathbf{p}_{j3})^2 \rho_{3j} / (\epsilon_0 \hbar \Omega_{pj}) = \chi_j^{(1)} + \sum_{l=1,2} \chi_{jl,\text{loc}}^{(3)} |\mathcal{E}_{pl}|^2 + \sum_{l=1,2} \chi_{jl,\text{nloc}}^{(3)} |\mathcal{E}_{pl}(\mathbf{r}')|^2 + \dots$. Here $\chi_j^{(1)}$ is linear susceptibility; $\chi_{jl,\text{loc}}^{(3)}$ ($j, l = 1, 2$) are local third-order nonlinear susceptibilities; $\chi_{jl,\text{nloc}}^{(3)}$

($j, l = 1, 2$) are nonlocal third-order nonlinear susceptibilities. Based on the CNLS equations (4), it is easy to get $\chi_{jl,loc}^{(3)} = 2c(\mathbf{e}_p \cdot \mathbf{p}_{j3})^2 W_{jl}/(\omega_{pj}\hbar^2)$ and $\chi_{jl,nloc}^{(3)} = 2c(\mathbf{e}_p \cdot \mathbf{p}_{j3})^2 \int d^2r' G_{jl}/(\omega_{pj}\hbar^2)$. With the system parameters given above, we get $\chi_{jl,loc}^{(3)} \sim 10^{-10} \text{ m}^2 \text{ V}^{-2}$, $\chi_{12,nloc}^{(3)} \approx \chi_{21,nloc}^{(3)} \approx \chi_{22,nloc}^{(3)} \approx \chi_{11,nloc}^{(3)} = (4.1 + i0.3) \times 10^{-7} \text{ m}^2 \text{ V}^{-2}$. Because the local Kerr nonlinearities are much smaller than the nonlocal ones, they will be neglected in the following.

III. CLONING OF HIGH-D OPTICAL BEAMS

A. High-D nonlocal optical solitons and vortices formed in the probe beam 1

We now consider optical cloning based on the CNLS equations (4a) and (4b). We assume that the probe field 1 is the one to be cloned and the probe field 2 is the one cloned. To implement the cloning, as a first step the probe field 1 must be prepared. We assume that the intensity of the probe field 1 is much stronger than that of the probe field 2, and thus the terms proportional to G_{12} and G_{22} in Eqs. (4a) and (4b) can be disregarded. Based on such consideration and for the convenience of latter numerical calculations, Eqs. (4a) and (4b) are written into the nondimensional form

$$i \frac{\partial u}{\partial s} + \tilde{\nabla}^2 u + \int d^2 \zeta' g_{11}(\tilde{\zeta} - \tilde{\zeta}') |u(\tilde{\zeta}', s)|^2 u = 0, \quad (5a)$$

$$i \frac{\partial v}{\partial s} + \tilde{\nabla}^2 v + \int d^2 \zeta' g_{21}(\tilde{\zeta} - \tilde{\zeta}') |u(\tilde{\zeta}', s)|^2 v = 0, \quad (5b)$$

with $(u, v) = (\Omega_{p1}, \Omega_{p2})/U_0$, $s = z/(2L_{\text{diff}})$, $\tilde{\zeta} = (\xi, \eta) = (x, y)/R_0$, $\tilde{\nabla}^2 = \partial^2/\partial \xi^2 + \partial^2/\partial \eta^2$, $d^2 \zeta' = d\xi' d\eta'$. Here $L_{\text{diff}} = \omega_p R_0^2/c$ is the typical diffraction length; R_0 and U_0 are, respectively, the typical transverse size and half Rabi frequency of the probe fields. The integral kernels (nondimensional nonlinear response functions) in the above equations are defined by $g_{11,21} = 2L_{\text{diff}} R_0^2 |U_0|^2 G_{11,21}$. With the system parameters given above, we have $L_{\text{diff}} \approx 0.87 \text{ mm}$ for $R_0 = 8 \mu\text{m}$.

From Eq. (5a) we see that the component u is controlled by a (2 + 1)D NNLS equation. For the parameter choice given in the last section, g_{11} is positive, i.e., the Kerr nonlinearity in Eq. (5a) is a self-focused one, and hence Eq. (5a) supports bright-soliton solutions. Since Eq. (5a) cannot be obtained analytically, we find its soliton solutions by virtue of numerical simulation. To this end, we assume the solution has the form

$$u(\tilde{\zeta}, s) = A(s) \exp \left[-\frac{|\tilde{\zeta}|^2}{2w^2(s)} \right] \exp \left[-iC(s) \frac{|\tilde{\zeta}|^2}{2w^2(s)} + i\phi(s) \right], \quad (6)$$

where $|\tilde{\zeta}|^2 = \xi^2 + \eta^2$, A is amplitude, w is transverse width, C is wavefront curvature, and ϕ is phase. All these parameters are assumed to depend on the nondimensional propagation distance s . A variational method is employed to solve Eq. (5a) by taking (6) as a trial solution. Through a Ritz optimization procedure, the beam energy E , defined by $E = \iint |u|^2 d\xi d\eta = \pi A^2 w^2$, is calculated as a function of the transverse width w , with the result shown in Fig. 2(a). We find that in the part represented by the solid red line where energy E is near the minimum the soliton solution is stable, while in

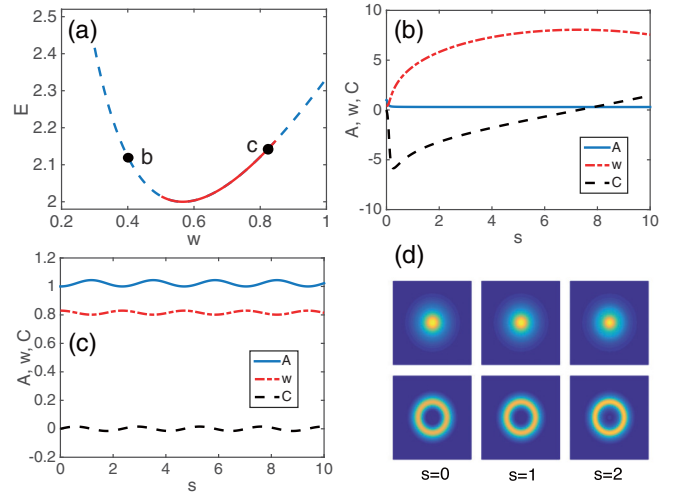


FIG. 2. High-D nonlocal optical soliton and vortices. (a) Soliton energy E as a function of the transverse width w . The solid red (dashed blue) part of the curve corresponds to the stable (unstable) soliton. (b) Numerical results of A (amplitude; solid blue line), w (transverse beam width; dot-dashed red line), and C (wavefront curvature; dashed black line) as functions of propagation distance $s = z/(2L_{\text{diff}})$. The initial condition is chosen from the point “b” in panel (a), i.e., $(A, C, w) = (1, 0, 0.4)$. (c) The same as (b) but with the initial condition chosen from the point “c” in the panel (a), i.e., $(A, C, w) = (1, 0, 0.83)$. (d) Normalized peak intensity of the soliton and vortex at different s . Upper row, soliton (the input beam is a Gaussian mode); lower row, vortex (the input beam is a Laguerre-Gaussian mode with $l = 1, p = 0$). All quantities in the figure are nondimensional.

the parts represented by the blue dashed lines where E is far away the minimum the soliton solution is unstable.

To prove the above conclusion further, two particular cases are investigated in detail. Shown in Fig. 2(b) is the result for the amplitude A (solid blue line), the transverse beam width w (dot-dashed red line), and the wavefront curvature C (dashed black line) of the soliton as functions of propagation distance $s = z/(2L_{\text{diff}})$. The initial condition is chosen from the point “b” [located in the unstable region of panel (a)], i.e., $(A, C, w) = (1, 0, 0.4)$. One sees that in this case the soliton is indeed unstable because the soliton parameters A , C , and w change very drastically during propagation. However, if the initial condition is chosen from the point “c” [located in the stable region of panel (a)], i.e., $(A, C, w) = (1, 0, 0.83)$, the soliton is quite stable because the soliton parameters A , C , and w can keep their values very close to the initial ones after propagating to a long distance.

To give a visual picture for the spatial distribution of the (2 + 1)D soliton during propagation, in the upper row of Fig. 2(d) we illustrate the peak-normalized intensity of the soliton for propagation distances, respectively, at $s = 0, 1, 2$, obtained by using an input beam with a Gaussian mode. We see that the soliton has no obvious deformation during propagation.

The energy flux associated with an optical beam can be estimated by a Poynting vector integrated over the transverse area of the beam [38]. For the soliton given in the upper part

of Fig. 2(d), we obtain

$$P \approx 4.4 \mu W, \quad (7)$$

which means that a very low input power is needed for generating the soliton. The physical reason for such low generation power of the soliton is due to the giant nonlocal Kerr nonlinearities contributed by the Rydberg-EIT in the system.

One can also find stable vortex solutions of the $(2+1)$ D NNLS equation (5a) by virtue of a variational method-based numerical simulation. Such solutions have also extremely low generation power and are quite stable in some specific parameter regions. For instance, one can choose the input to be the Laguerre-Gaussian (LG) mode [40]

$$u(\vec{\zeta}, s=0) = \frac{u_0}{w_0} \left(\frac{\sqrt{2|\vec{\zeta}|^2}}{w_0} \right)^{|l|} \exp\left(-\frac{|\vec{\zeta}|^2}{w_0^2}\right) \times L_p^{|l|} \left[\frac{2|\vec{\zeta}|^2}{w_0^2} \right] \exp(il\varphi), \quad (8)$$

where $L_p^{|l|}$ is a generalized LG polynomial with l (p) the azimuthal (radial) index, u_0 (w_0) is the beam amplitude (waist), and φ is the azimuthal angle with $\varphi \in [0, 2\pi]$. The related analysis is similar to that given above but omitted here for saving space. Shown in the lower row of Fig. 2(d) is the result for the propagation of an optical vortex, where the input beam used is a LG mode with $l = 1$ and $p = 0$, for $u_0 = 2.48$ and $w_0 = 1$. One sees that it is quite stable during propagation.

The physical reason for the stability of the $(2+1)$ D soliton and vortices obtained here is the strong and long-range nonlocal Kerr nonlinearity coming from the Rydberg-Rydberg interaction between atoms, which not only can suppress the diffraction in transverse directions but also can arrest the spread or collapse of high-D nonlinear optical beams [40].

B. Cloning of high-D optical beams from the probe field 1 onto the probe field 2

Now we turn to consider the second step of the cloning of optical beams, i.e., to map the wavelshape of the probe field 1 onto that of the probe field 2. The physical mechanism of the optical cloning considered here is as follows. After the probe field 1 (i.e., u , the optical beam to be cloned) is prepared as a stable $(2+1)$ D wave packet (as described in the last subsection), due to the nonlocal cross-Kerr nonlinearity it will play a role as a nonlocal external potential to the probe field 2 (i.e., v , the optical beam cloned) [see Eq. (5b)]. Then the probe field 2 is confined and guided stably by the nonlocal external potential contributed by the probe field 1. As a result, the probe field 2 acquires a stable $(2+1)$ D spatial distribution (copy) of the probe field 1. In order to have a better illustration, we carry out a numerical investigation based on the reduced CNLS equations (5a) and (5b). Moreover, two examples are considered in the following.

The first example is the cloning of a $(2+1)$ D optical vortex. At the beginning, a stable optical vortex (with $l = 1$ and $p = 0$) is obtained in the probe field 1 through solving Eq. (5a), with the result shown by the upper row of Fig. 1(c), where the normalized peak intensity is illustrated

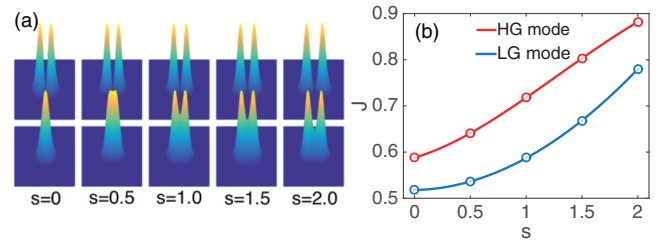


FIG. 3. Cloning of high-D optical beams. (a) Normalized peak intensities of the probe field 1 (i.e., the optical beam to be cloned; upper row) and the probe field 2 (i.e., the optical beam cloned; lower row) for different propagation distance $s = z/(2L_{\text{diff}})$. The input of the probe field 1 is a Hermite-Gaussian mode (with $m = 1, n = 0$). The input of the probe field 2 is a Gaussian mode. (b) Waveshape fidelity J as a function of s for the cloning of the Laguerre-Gaussian mode (blue line) and for the Hermite-Gaussian mode (red line), respectively. All quantities in the figure are nondimensional.

for different propagation distances, i.e., $s = z/(2L_{\text{diff}}) = 0, 0.5, 1.0, 1.5, 2.0$, respectively. Then, this optical vortex is cloned onto the probe field 2 [controlled by Eq. (5b)] when it propagates to the position $s = 2.0$. In the simulation, the initial input wavelshape of the probe field 2 is taken to be a hyperbolic secant one, i.e., $v(\vec{\zeta}, s=0) = v_0 \text{sech}(|\vec{\zeta}|/w_0)$, with $v_0 = 0.35$ and $w_0 = 1$. From the figure, we see that the probe field 2 acquires almost the same wavelshape as the probe field 1.

The quality of the optical intensity cloning realized above can be characterized by the overlap integral of the input intensity of the probe field 1 (at position $s = 0$) and the output intensity of the probe field 2 (at position s), which is called the waveshape fidelity J , defined by [40]

$$J(s) = \frac{\left| \int_{-\infty}^{+\infty} d^2\zeta v(\vec{\zeta}, s) |u(\vec{\zeta}, s=0)|^2 \right|}{\int_{-\infty}^{+\infty} d^2\zeta |v(\vec{\zeta}, s)|^2 \int_{-\infty}^{+\infty} d^2\zeta |u(\vec{\zeta}, s=0)|^2}. \quad (9)$$

Illustrated by the blue line in Fig. 3(b) is the waveshape fidelity J as a function of s for the cloning of the optical vortex (i.e., the LG mode with $l = 1, p = 0$), presented in Fig. 1(c). At the propagation distance $s = 2$, we obtain $J \approx 78\%$, which means that the wavelshape of the optical vortex in the probe field 1 can be well cloned onto the wavelshape of the probe field 2 with a high fidelity.

As a second example, we consider a numerical simulation on the cloning of a Hermite-Gaussian (HG) mode:

$$u(\vec{\zeta}, s=0) = u_0 H_m \left(\frac{\sqrt{2}\xi}{w_0} \right) H_n \left(\frac{\sqrt{2}\eta}{w_0} \right) \exp\left(-\frac{|\vec{\zeta}|^2}{w_0^2}\right), \quad (10)$$

where H_m is the Hermite polynomial of order m , and u_0 and w_0 are the mode amplitude and waist, respectively. In the simulation, we choose $m = 1, n = 0$, and $u_0 = 7.8, w_0 = 1$; the input of the probe field 2 is a Gaussian beam $v(\vec{\zeta}, s=0) = v_0 \exp[-|\vec{\zeta}|^2/w_0^2]$, with $v_0 = 2$ and $w_0 = 1$. Shown in Fig. 3(a) is peak-normalized intensities of the probe field 1 (i.e., the optical beam to be cloned; upper row) and the probe field 2 (i.e., the optical beam cloned; lower row) for different nondimensional propagation distance s . We see that the probe

field 1 propagates very stably due to the role played by the nonlocal self-Kerr nonlinearity in the system; for a larger propagation distance, the waveshape of the probe field 2 is changed from the Gaussian one into that of the probe field 1 (i.e., the HG one). Figure 3(b) shows J as a function of s ; at $s = 2$, one obtains $J \approx 88\%$, which means that the optical cloning has a high waveshape fidelity.

To make a comparison, a numerical simulation for the cloning of the same optical modes is also carried out for an atomic gas working under a normal double EIT, which can be realized by the present system with a lower atomic density (i.e., the Rydberg-Rydberg interaction can be neglected). The result shows that, though in such a case the optical cloning is possible, the waveshape fidelity J is much lower than in the case of the double Rydberg-EIT (i.e., the Rydberg-Rydberg interaction cannot be neglected). For example, for the cloning of the HG mode with $(m, n) = (1, 0)$ via the normal double EIT we obtain $J \approx 9\%$ at propagation distance $s = 2$ (i.e., $z = 3.48$ mm), which is much lower than that obtained via the double Rydberg-EIT ($J \approx 88\%$) for the same propagation distance. Consequently, the optical cloning using the double Rydberg-EIT is much better than that using the normal double EIT. The physical reason for this lies in the fact that the existence of the giant nonlocal self-Kerr and cross-Kerr nonlinearities contributed by the strong Rydberg-Rydberg interaction allows not only the formation and stable propagation but also the high-fidelity cloning of high-D nonlinear optical beams in the system.

C. Manipulation of the optical cloning

The cloning of the high-D optical beams demonstrated above can be actively manipulated by changing the system parameters. In particular, the nonlocality degree of the Kerr nonlinearities in the system, defined by

$$\sigma = R_b/R_0, \quad (11)$$

may significantly influence the waveshape fidelity of the cloning. Here $R_b = (|C_6/\delta_{\text{EIT}}|)^{1/6}$ is the Rydberg blockade radius, with $\delta_{\text{EIT}} = |\Omega_c|^2/|\Delta_3|$ the linewidth of the EIT transmission spectrum (for $|\Delta_3| \gg \Gamma_3$) [31,32]. Based on our system parameters, we have $R_b \approx 3.9 \mu\text{m}$. One can obtain different σ by tuning R_0 (the typical transverse size of the probe fields), Δ_3 , and Ω_c , etc., and hence realize different optical cloning with different waveshape fidelities.

Shown in Fig. 4(a) is the waveshape fidelity J for the cloning of the LG mode (with $l = 1$ and $p = 0$) as a function of nonlocality degree σ for $s = 2$. The upper inset in the figure shows the input intensity distribution of the probe beam 2; the lower insets give the output intensity distributions of the probe beam 2 at $s = 2$ for the nonlocality degree $\sigma = 0.5$ (part A), $\sigma = 0.7$ (part B), and $\sigma = 2.7$ (part C), respectively. From the figure, we see that starting from $\sigma = 0$ the waveshape fidelity J increases rapidly as σ increases, and reaches its maximum $J_{\text{max}} \approx 79\%$ at $\sigma \approx 0.8$; then, it turns to decrease with a further increasing of σ .

Shown in Fig. 4(b) is the same as that in Fig. 4(a) but for the cloning of the HG mode (with $m = 1$, $n = 0$). The input intensity distribution of the probe field 2 and the output intensity distributions of the probe field 2 are also illustrated

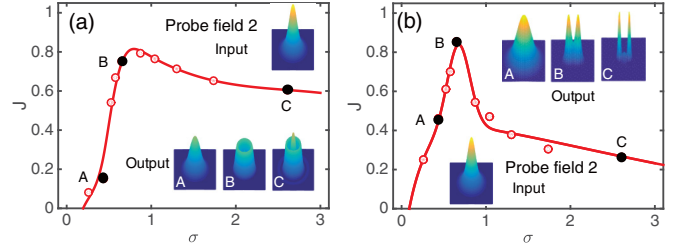


FIG. 4. Manipulation of the optical cloning. (a) Waveshape fidelity J for the Laguerre-Gaussian mode ($l = 1$, $p = 0$) as a function of nonlocality degree σ for the propagation distance $s = 2.0$. Upper inset: The input intensity distribution of the probe field 2. Lower insets: The output intensity distributions of the probe field 2 at $s = 2.0$ for the nonlocality degree $\sigma = 0.5$ (part A), $\sigma = 0.7$ (part B), and $\sigma = 2.7$ (part C), respectively. (b) The same as (a) but for the Hermite-Gaussian mode ($m = 1$, $n = 0$). The input intensity distribution of the probe field 2 (lower inset) and the output intensity distributions of the probe field 2 (upper insets) are also shown. All quantities in the figure are nondimensional.

by the lower inset and the upper insets, respectively. From the figure, one can also obtain similar conclusions as those gained from Fig. 4(a).

The reason that the waveshape fidelity J of the cloning has the significant dependence on the nonlocality degree σ can be understood as follows. At one limit where σ is small, the nonlocal Kerr nonlinearities of the system become local ones, i.e., the nonlinear response functions in Eqs. (5a) and (5b) are reduced to the form $g_{11,21}(\vec{\zeta} - \vec{\zeta}') \rightarrow g_{11,21}^{(0)}\delta(\vec{\zeta} - \vec{\zeta}')$ (here $g_{11,21}^{(0)}$ are constants), which makes (5a) and (5b) become local nonlinear equations. Because the high-D soliton and vortex solutions of such equations are highly unstable due to the transverse instability induced by diffraction, the cloning of high-D optical solitons and vortices is thus not possible (or the fidelity is very low). At another limit σ is very large. In this case the nonlinear terms in Eqs. (5a) and (5b) can be approximated, respectively, by $g_{11}(\vec{\zeta} = 0)P_0 u$ and $g_{21}(\vec{\zeta} = 0)P_0 v$, where $P_0 = \iint d^2\zeta |u|^2$ is the power of the probe field 1. As a result, Eqs. (5a) and (5b) become uncoupled linear equations, which means that the cloning from one probe field onto the other one is also not possible. Consequently, only for the situation where the nonlocality degree σ takes finite values, the cloning of high-D optical beams is possible and it may acquire a maximum waveshape fidelity for some particular values of σ .

IV. MULTITIMES AND MULTICOMPONENTS CLONING OF HIGH-D OPTICAL BEAMS

A. Multitimes cloning of high-D optical beams

Now we generalize the foregoing approach of single-time cloning to multitimes cloning based on also the controllability of the system, which is useful to allow us to acquire multiple copies by the cloning. As an example, here we consider the two-times cloning of the HG mode with $m = 1$ and $n = 0$, with the result shown in Fig. 5, which is obtained through a numerical simulation based on Eqs. (5a) and (5b).

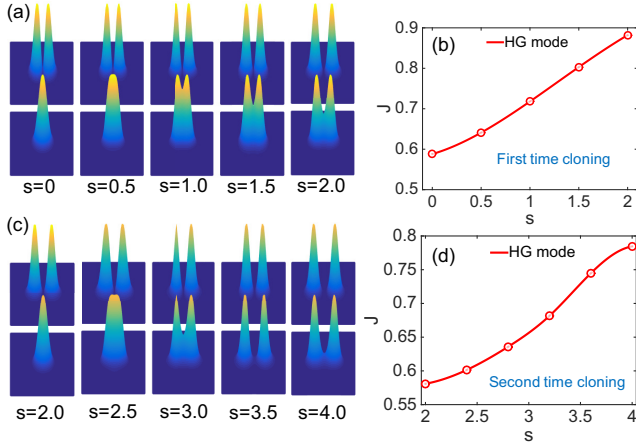


FIG. 5. Two-times cloning of high-D optical beams. (a) Normalized peak intensity distributions of the probe field 1 (the optical beam to be cloned; upper row) and probe field 2 (the optical beam cloned; lower row) as functions of propagation distance s during the stage of the first-time cloning, implemented in the propagation interval between $s = 0$ and 2.0. The inputs of the probe field 1 and probe field 2 are the Hermite-Gaussian mode ($m = 1, n = 0$) and Gaussian mode, respectively. (b) Waveshape fidelity J as a function of s for the first-time cloning. (c) The same as (a) but for the second-time cloning, implemented in the propagation interval between $s = 2.0$ and 4.0. (d) Waveshape fidelity J as a function of s for the second-time cloning. All quantities in the figure are nondimensional.

Given in Fig. 5(a) are normalized peak intensity distributions of the probe field 1 (i.e., the optical beam to be cloned; upper row) and probe field 2 (i.e., the optical beam cloned; lower row) as functions of nondimensional propagation distance s during the stage of the first-time cloning, implemented in the propagation interval between $s = 0$ and 2.0. The inputs of the probe field 1 and probe field 2 are, respectively, the Hermite-Gaussian mode ($m = 1, n = 0$) and Gaussian mode, with parameters the same as those used in Fig. 3(a). The panel (b) of Fig. 5 gives the waveshape fidelity J as a function of s for the first-time cloning, the value of which is 88% at $s = 2.0$.

To have a second-time cloning, we switch off the probe field 2 but keep the probe field 1 propagating on; then by inputting a new probe field 2 with a Gaussian mode, we can obtain a new probe field 2 that is the cloning of the probe field 1. Illustrated in Fig. 5(c) are the normalized peak intensities of the probe field 1 (upper row) and probe field 2 (lower row) during the stage of the second-time cloning, implemented in the propagation interval between $s = 2.0$ and 4.0. The panel (d) of Fig. 5 shows the waveshape fidelity J as a function of s for the second-time cloning, which has the value of 78% at $s = 4.0$. In a similar way, the cloning with more than two copies may also be possible subsequently if the times of the cloning is larger than two.

B. Multicomponents cloning of high-D optical beams

Finally, we further generalize the single-component cloning to multicomponents cloning by extending the model given by Fig. 1(a), which allows us to acquire many copies by the cloning simultaneously. To be specific, we consider

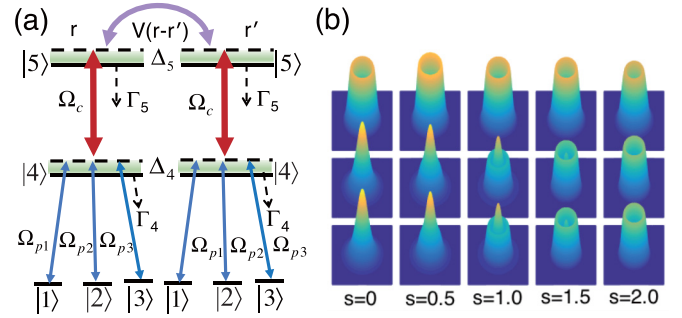


FIG. 6. Two-components cloning of high-D optical beams. (a) Energy-level diagram and excitation scheme of the inverted Ψ -type five-level system for realizing the two-components cloning. (b) Peak-normalized intensities of the probe field 1 (the optical beam to be cloned; upper row), probe field 2 (the optical beam cloned; middle row), and probe field 3 (the optical beam cloned; lower row) for different propagation distance s . The input of the probe field 1 is a Laguerre-Gaussian mode with $l = 1$ and $p = 0$. The input of the both probe field 2 and probe field 3 have the waveshape of hyperbolic secant mode. All quantities in the right part of the figure are nondimensional.

an inverted Ψ -type five-level system, with the energy-level diagram and excitation scheme shown in Fig. 6(a). Here three weak probe fields with half Rabi frequencies Ω_{p1} , Ω_{p2} , and Ω_{p3} couple, respectively, the transitions $|1\rangle \leftrightarrow |4\rangle$, $|2\rangle \leftrightarrow |4\rangle$, and $|3\rangle \leftrightarrow |4\rangle$; the strong control field with half Rabi frequency Ω_c couples the transition $|4\rangle \leftrightarrow |5\rangle$, with $|5\rangle$ a Rydberg state. The nondimensional nonlinear equations governing the propagation of Ω_{pj} ($j = 1, 2, 3$) read

$$i \frac{\partial u}{\partial s} + \tilde{\nabla}^2 u + \iint d^2 \zeta' g_{11}(\vec{\zeta} - \vec{\zeta}') |u(\vec{\zeta}', s)|^2 u = 0, \quad (12a)$$

$$i \frac{\partial v}{\partial s} + \tilde{\nabla}^2 v + \iint d^2 \zeta' g_{21}(\vec{\zeta} - \vec{\zeta}') |u(\vec{\zeta}', s)|^2 v = 0, \quad (12b)$$

$$i \frac{\partial w}{\partial s} + \tilde{\nabla}^2 w + \iint d^2 \zeta' g_{31}(\vec{\zeta} - \vec{\zeta}') |u(\vec{\zeta}', s)|^2 w = 0, \quad (12c)$$

where $w = \Omega_{p3}/U_0$ and $g_{31} = 2L_{\text{diff}} R_0^2 |U_0|^2 G_{31} \approx g_{21}$; the definitions of u , v , g_{11} , and g_{21} are the same as those given in Eqs. (5a) and (5b).

Shown in Fig. 6(b) are normalized peak intensity distributions of the probe field 1 (the optical beam to be cloned; upper row), probe field 2 (the optical beam cloned; middle row), and probe field 3 (the optical beam cloned; lower row) for different propagation distance s . The input of the probe field 1 is a LG mode with $l = 1$ and $p = 0$; the input of both the probe field 2 and probe field 3 have waveshape of hyperbolic secant mode. The result is obtained by a numerical simulation based on Eqs. (12a), (12b), and (12c). We see that the probe field 1 propagates stably; the probe field 2 and probe field 3 change their shapes first and then they acquire the similar waveshape as that of the probe field 1 after propagation to some positions. Especially, at $s = 2.0$ the probe field 2 and probe field 3 can acquire nearly the same waveshape as that

of probe field 1, which means that two copies by the cloning have been realized. Note that the cloning with more than two copies may also be acquired at the same time if the number of the probe fields used in the system is larger than 2.

V. SUMMARY

In this paper we have proposed a scheme for realizing the cloning of high-D optical beams by taking the Rydberg atomic gas as an effective optical cloning device. We have shown that strong Rydberg-Rydberg interaction between atoms can map to two probe laser fields, which may gain giant, nonlocal Kerr nonlinearities through the mechanism of the double Rydberg-EIT. We have also shown when the double Rydberg-EIT works in the dispersive regime the system supports stable high-D optical solitons and vortices, which may be obtained at extremely low light power. By virtue of the cross-Kerr nonlinearities, these optical solitons and vortices prepared in one probe beam can be cloned onto another one with very high waveshape fidelity. Moreover, the cloning of high-D optical beams may be actively manipulated by tuning the nonlocality degree of the Kerr nonlinearities. In addition, we have demonstrated that multitudes and multicomponents cloning of such optical beams can be realized, which allows us to acquire multiple copies of high-D optical beams by exploiting such a cloning.

The scheme presented above can be generalized to realize the cloning of high-D optical pulses and optical images. The high-fidelity and controllable cloning of high-D optical fields reported in this paper are not only of fundamental interest for the development of nonlocal nonlinear optics but also promising for practical applications in all-optical information processing and transmission, including diffractionless biological and medical imaging [33,34].

ACKNOWLEDGMENTS

This work was supported by National Natural Science Foundation of China under Grants No. 11974117 and No. 11975098.

APPENDIX A: EXPLICIT EXPRESSION OF THE OPTICAL BLOCH EQUATION

The dynamics of the atomic motion is governed by the optical Bloch equation

$$\frac{\partial \hat{\rho}}{\partial t} = -\frac{i}{\hbar} [\hat{H}, \hat{\rho}] - \Gamma [\hat{\rho}]. \quad (\text{A1})$$

Here $\hat{\rho}$ is the DM describing the atomic population and coherence, with the DM elements defined by $\rho_{\alpha\beta} \equiv \langle \hat{S}_{\alpha\beta} \rangle$ [46]; Γ is the relaxation matrix describing the spontaneous emission and dephasing.

Based on the Hamiltonian \hat{H} given in the main text, we obtain the explicit expression of the optical Bloch equation with the following form:

$$i\frac{\partial}{\partial t}\rho_{11} + i\Gamma_{21}\rho_{11} - i\Gamma_{13}\rho_{33} + \Omega_{p1}^*\rho_{31} - \Omega_{p1}\rho_{13} = 0, \quad (\text{A2a})$$

$$i\frac{\partial}{\partial t}\rho_{22} - i\Gamma_{21}\rho_{11} - i\Gamma_{23}\rho_{33} + \Omega_{p2}^*\rho_{32} - \Omega_{p2}\rho_{23} = 0, \quad (\text{A2b})$$

$$i\frac{\partial}{\partial t}\rho_{33} - i\Gamma_{34}\rho_{44} + i\Gamma_{3\rho_{33}} - \Omega_{p1}^*\rho_{31} + \Omega_{p1}\rho_{13} - \Omega_{p2}^*\rho_{32} + \Omega_{p2}\rho_{23} + \Omega_c^*\rho_{43} - \Omega_c\rho_{34} = 0, \quad (\text{A2c})$$

$$i\frac{\partial}{\partial t}\rho_{44} + i\Gamma_{34}\rho_{44} - \Omega_c^*\rho_{43} + \Omega_c\rho_{34} = 0, \quad (\text{A2d})$$

for the diagonal elements, and

$$\left(i\frac{\partial}{\partial t} + d_{21}\right)\rho_{21} + \Omega_{p2}^*\rho_{31} - \Omega_{p1}\rho_{23} = 0, \quad (\text{A3a})$$

$$\left(i\frac{\partial}{\partial t} + d_{31}\right)\rho_{31} + \Omega_c^*\rho_{41} + \Omega_{p1}(\rho_{11} - \rho_{33}) + \Omega_{p2}\rho_{21} = 0, \quad (\text{A3b})$$

$$\left(i\frac{\partial}{\partial t} + d_{32}\right)\rho_{32} + \Omega_c^*\rho_{42} + \Omega_{p2}(\rho_{22} - \rho_{33}) + \Omega_{p1}\rho_{12} = 0, \quad (\text{A3c})$$

$$\left(i\frac{\partial}{\partial t} + d_{41}\right)\rho_{41} + \Omega_c\rho_{31} - \Omega_{p1}\rho_{43} - \mathcal{N}_a \int d^3r' V(\mathbf{r}' - \mathbf{r})\rho_{44,41}(\mathbf{r}', \mathbf{r}, t) = 0, \quad (\text{A3d})$$

$$\left(i\frac{\partial}{\partial t} + d_{42}\right)\rho_{42} + \Omega_c\rho_{32} - \Omega_{p2}\rho_{43} - \mathcal{N}_a \int d^3r' V(\mathbf{r}' - \mathbf{r})\rho_{44,42}(\mathbf{r}', \mathbf{r}, t) = 0, \quad (\text{A3e})$$

$$\left(i\frac{\partial}{\partial t} + d_{43}\right)\rho_{43} - \Omega_{p1}^*\rho_{41} - \Omega_{p2}^*\rho_{42} + \Omega_c(\rho_{33} - \rho_{44}) - \mathcal{N}_a \int d^3r' V(\mathbf{r}' - \mathbf{r})\rho_{44,43}(\mathbf{r}', \mathbf{r}, t) = 0 \quad (\text{A3f})$$

for the nondiagonal elements. Here $d_{\alpha\beta} = \Delta_\alpha - \Delta_\beta + i\gamma_{\alpha\beta}$; $\gamma_{\alpha\beta} = (\Gamma_\alpha + \Gamma_\beta)/2 + \gamma_{\alpha\beta}^{\text{col}}$, $\Gamma_\alpha = \sum_{\alpha < \beta} \Gamma_{\alpha\beta}$, with $\Gamma_{\alpha\beta}$ the spontaneous emission decay rate from $|\beta\rangle$ to $|\alpha\rangle$ and $\gamma_{\alpha\beta}^{\text{col}}$ the dephasing rate reflecting the loss of the phase coherence between $|\alpha\rangle$ and $|\beta\rangle$; Γ_{21} is a rate of population exchange between $|1\rangle$ and $|2\rangle$; $\rho_{44,4\alpha}(\mathbf{r}', \mathbf{r}, t) = \langle \hat{S}_{44}(\mathbf{r}', t)\hat{S}_{4\alpha}(\mathbf{r}, t) \rangle$ are two-body DM elements; the interaction between two Rydberg atoms, respectively, at positions \mathbf{r} and \mathbf{r}' is described by the potential $V_{\text{vdw}}(\mathbf{r}' - \mathbf{r}) = -\hbar C_6/|\mathbf{r}' - \mathbf{r}|^6$, with C_6 the dispersion parameter.

APPENDIX B: SOLUTION OF THE MB EQUATIONS

1. Solutions of one-body density-matrix elements

We assume that atoms are initially populated in $|1\rangle$ and $|2\rangle$. Since the two probe fields are much weaker than the control field, we can take Ω_{pj} ($\sim \varepsilon$) as an expansion parameter and the perturbation expansion $\rho_{\alpha\alpha} = \rho_{\alpha\alpha}^{(0)} + \varepsilon\rho_{\alpha\alpha}^{(1)} + \varepsilon^2\rho_{\alpha\alpha}^{(2)} + \dots$ ($\alpha = 1, 2, 3, 4$), and $\rho_{\alpha\beta} = \varepsilon\rho_{\alpha\beta}^{(1)} + \varepsilon^2\rho_{\alpha\beta}^{(2)} + \dots$ ($\alpha = 2, 3, 4; \beta = 1, 2, 3; \alpha > \beta$). Substituting the above expansions into Eqs. (A2), we obtain a set of linear but inhomogeneous equations which can be solved order by order [47].

a. First-order solutions

At the first order, the solutions of $\rho_{31}^{(1)}$, $\rho_{32}^{(1)}$, $\rho_{41}^{(1)}$, and $\rho_{42}^{(1)}$ are given by

$$\rho_{31}^{(1)} = \frac{d_{41}\rho_{11}^{(0)}}{|\Omega_c|^2 - d_{31}d_{41}}\Omega_{p1} \equiv a_{31}^{(1)}\Omega_{p1}, \quad (\text{B1a})$$

$$\rho_{41}^{(1)} = \frac{-\Omega_c\rho_{11}^{(0)}}{|\Omega_c|^2 - d_{31}d_{41}}\Omega_{p1} \equiv a_{41}^{(1)}\Omega_{p1}, \quad (\text{B1b})$$

$$\rho_{32}^{(1)} = \frac{d_{42}\rho_{22}^{(0)}}{|\Omega_c|^2 - d_{32}d_{42}}\Omega_{p2} \equiv a_{32}^{(1)}\Omega_{p2}, \quad (\text{B1c})$$

$$\rho_{42}^{(1)} = \frac{-\Omega_c\rho_{22}^{(0)}}{|\Omega_c|^2 - d_{32}d_{42}}\Omega_{p2} \equiv a_{42}^{(1)}\Omega_{p2}, \quad (\text{B1d})$$

and other $\rho_{\alpha\beta}^{(1)}$ are zero.

b. Second-order solutions

At the second order, $\rho_{33}^{(2)}$, $\rho_{44}^{(2)}$, $\rho_{43}^{(2)}$, and $\rho_{34}^{(2)}$ can be solved by the equation

$$\begin{bmatrix} i\Gamma_3 & -i\Gamma_{34} & \Omega_c^* & -\Omega_c \\ 0 & i\Gamma_{34} & -\Omega_c^* & \Omega_c \\ \Omega_c & -\Omega_c & d_{43} & 0 \\ \Omega_c^* & -\Omega_c^* & 0 & d_{43}^* \end{bmatrix} \begin{bmatrix} \rho_{33}^{(2)} \\ \rho_{44}^{(2)} \\ \rho_{43}^{(2)} \\ \rho_{34}^{(2)} \end{bmatrix} = \begin{bmatrix} 2i\text{Im}(a_{31}^{(1)}) \\ 0 \\ a_{41}^{(1)} \\ a_{14}^{(1)} \end{bmatrix} |\Omega_{p1}|^2 + \begin{bmatrix} 2i\text{Im}(a_{32}^{(1)}) \\ 0 \\ a_{42}^{(1)} \\ a_{24}^{(1)} \end{bmatrix} |\Omega_{p2}|^2. \quad (\text{B2})$$

The solutions for $\rho_{33}^{(2)}$, $\rho_{44}^{(2)}$, $\rho_{43}^{(2)}$, and $\rho_{34}^{(2)}$ read

$$\rho_{33}^{(2)} = a_{33,1}^{(2)}|\Omega_{p1}|^2 + a_{33,2}^{(2)}|\Omega_{p2}|^2, \quad (\text{B3a})$$

$$\rho_{44}^{(2)} = a_{44,1}^{(2)}|\Omega_{p1}|^2 + a_{44,2}^{(2)}|\Omega_{p2}|^2, \quad (\text{B3b})$$

$$\rho_{43}^{(2)} = a_{43,1}^{(2)}|\Omega_{p1}|^2 + a_{43,2}^{(2)}|\Omega_{p2}|^2, \quad (\text{B3c})$$

$$\rho_{34}^{(2)} = a_{34,1}^{(2)}|\Omega_{p1}|^2 + a_{34,2}^{(2)}|\Omega_{p2}|^2. \quad (\text{B3d})$$

The solutions of $\rho_{11}^{(2)}$, $\rho_{22}^{(2)}$, and $\rho_{21}^{(2)}$ read

$$\begin{aligned} \rho_{21}^{(2)} &= \frac{1}{d_{21}}[\rho_{23}^{(1)}\Omega_{p1} - \rho_{31}^{(1)}\Omega_{p2}^*] \\ &= \frac{1}{d_{21}}[a_{23}^{(1)} - a_{31}^{(1)}]\Omega_{p1}\Omega_{p2}^*, \end{aligned} \quad (\text{B4a})$$

$$\begin{aligned} \rho_{11}^{(2)} &= \frac{\Gamma_{13}a_{33,1}^{(2)} + i(a_{31}^{(1)} - a_{13}^{(1)})}{\Gamma_{21}}|\Omega_{p1}|^2 + \frac{\Gamma_{13}a_{33,2}^{(2)}}{\Gamma_{21}}|\Omega_{p2}|^2 \\ &\equiv a_{11,1}^{(2)}|\Omega_{p1}|^2 + a_{11,2}^{(2)}|\Omega_{p2}|^2, \end{aligned} \quad (\text{B4b})$$

$$\begin{aligned} \rho_{22}^{(2)} &= -(a_{11,1}^{(2)} + a_{33,1}^{(2)} + a_{44,1}^{(2)})|\Omega_{p1}|^2 \\ &\quad - (a_{11,2}^{(2)} + a_{33,2}^{(2)} + a_{44,2}^{(2)})|\Omega_{p2}|^2 \\ &\equiv a_{22,1}^{(2)}|\Omega_{p1}|^2 + a_{22,2}^{(2)}|\Omega_{p2}|^2. \end{aligned} \quad (\text{B4c})$$

c. Third-order solutions

At the third order, the solutions of $\rho_{31}^{(3)}$ and $\rho_{32}^{(3)}$ read

$$\begin{aligned} \rho_{31}^{(3)} &= a_{31,1}^{(3)}|\Omega_{p1}|^2\Omega_{p1} + a_{31,2}^{(3)}|\Omega_{p2}|^2\Omega_{p1} \\ &\quad + \mathcal{N}_a \int d^3r' V(\mathbf{r}' - \mathbf{r}) a_{31,3}^{(3)}(\mathbf{r}', \mathbf{r}, t) |\Omega_{p1}(\mathbf{r}')|^2 \Omega_{p1}(\mathbf{r}) \\ &\quad + \mathcal{N}_a \int d^3r' V(\mathbf{r}' - \mathbf{r}) a_{31,4}^{(3)}(\mathbf{r}', \mathbf{r}, t) |\Omega_{p2}(\mathbf{r}')|^2 \Omega_{p1}(\mathbf{r}), \end{aligned} \quad (\text{B5a})$$

$$\begin{aligned} \rho_{32}^{(3)} &= a_{32,1}^{(3)}|\Omega_{p1}|^2\Omega_{p2} + a_{32,2}^{(3)}|\Omega_{p2}|^2\Omega_{p2} \\ &\quad + \mathcal{N}_a \int d^3r' V(\mathbf{r}' - \mathbf{r}) a_{32,3}^{(3)}(\mathbf{r}', \mathbf{r}, t) |\Omega_{p2}(\mathbf{r}')|^2 \Omega_{p1}(\mathbf{r}) \\ &\quad + \mathcal{N}_a \int d^3r' V(\mathbf{r}' - \mathbf{r}) a_{32,4}^{(3)}(\mathbf{r}', \mathbf{r}, t) |\Omega_{p2}(\mathbf{r}')|^2 \Omega_{p2}(\mathbf{r}), \end{aligned} \quad (\text{B5b})$$

with the coefficients given by

$$a_{31,l}^{(3)} = \frac{\Omega_c^* a_{43,l}^{(2)} + d_{41}(a_{11,l}^{(2)} - a_{33,l}^{(2)} - \delta_{2l} a_{21}^{(2)})}{|\Omega_c|^2 - d_{31}d_{41}}, \quad (\text{B6a})$$

$$a_{32,l}^{(3)} = \frac{\Omega_c^* a_{43,l}^{(2)} + d_{42}(a_{22,l}^{(2)} - a_{33,l}^{(2)} + \delta_{1l} a_{12}^{(2)})}{|\Omega_c|^2 - d_{32}d_{42}}, \quad (\text{B6b})$$

$$a_{31,l+2}^{(3)} = \frac{\Omega_c^* a_{44,41,l}^{(3)}}{|\Omega_c|^2 - d_{31}d_{41}}, \quad (\text{B6c})$$

$$a_{32,l+2}^{(3)} = \frac{\Omega_c^* a_{44,42,l}^{(3)}}{|\Omega_c|^2 - d_{32}d_{42}}, \quad (\text{B6d})$$

where $l = 1, 2$.

2. Solutions of two-body density-matrix elements

Note that to get the expressions of the third-order solutions of the one-body DM elements, one must solve the equations of motion for the two-body MD elements $\langle \hat{S}_{\alpha\beta} \hat{S}_{\mu\nu} \rangle \equiv \rho_{\alpha\beta,\mu\nu}^{(2)}$. For example, the equations of two-body DM elements $\langle \hat{S}_{44} \hat{S}_{41} \rangle$ and $\langle \hat{S}_{44} \hat{S}_{42} \rangle$ read

$$\begin{aligned} &\left(i \frac{\partial}{\partial t} + d_{41} + i\Gamma_{34} - V(\mathbf{r}' - \mathbf{r}) \right) \langle \hat{S}_{44} \hat{S}_{41} \rangle - \Omega_c^* \langle \hat{S}_{43} \hat{S}_{41} \rangle \\ &\quad + \Omega_c (\langle \hat{S}_{34} \hat{S}_{41} \rangle + \langle \hat{S}_{44} \hat{S}_{31} \rangle) - \Omega_{p1} \langle \hat{S}_{44} \hat{S}_{43} \rangle \\ &\quad - \mathcal{N}_a \int d^3r'' \langle \hat{S}_{44}(\mathbf{r}'', t) \hat{S}_{44}(\mathbf{r}', t) \hat{S}_{41}(\mathbf{r}, t) \rangle V(\mathbf{r}'' - \mathbf{r}) = 0, \end{aligned} \quad (\text{B7a})$$

$$\begin{aligned} &\left(i \frac{\partial}{\partial t} + d_{42} + i\Gamma_{34} - V(\mathbf{r}' - \mathbf{r}) \right) \langle \hat{S}_{44} \hat{S}_{42} \rangle - \Omega_c^* \langle \hat{S}_{43} \hat{S}_{42} \rangle \\ &\quad + \Omega_c (\langle \hat{S}_{34} \hat{S}_{42} \rangle + \langle \hat{S}_{44} \hat{S}_{32} \rangle) - \Omega_{p2} \langle \hat{S}_{44} \hat{S}_{43} \rangle \\ &\quad - \mathcal{N}_a \int d^3r'' \langle \hat{S}_{44}(\mathbf{r}'', t) \hat{S}_{44}(\mathbf{r}', t) \hat{S}_{42}(\mathbf{r}, t) \rangle V(\mathbf{r}'' - \mathbf{r}) = 0. \end{aligned} \quad (\text{B7b})$$

From Eqs. (B7), one sees that the equations for the two-body DM elements involve three-body DM elements; similarly, the equations for three-body DM elements will

involve four-body DM elements, etc. As a result, one obtains an infinite hierarchy of equations of motion for the DM elements of one-body, two-body, \dots , N -body, \dots , equations, which must be solved simultaneously. Apparently, to make the problem tractable a truncation approximation for the hierarchy

must be taken. Here we assume that, for the atomic density considered in the main text, the one- and two-body correlations of the atoms should be fully taken into account but the three-body DM elements can be factorized in the following way [48]:

$$\begin{aligned} \langle \hat{S}_{\alpha\beta}(\mathbf{r}'', t) \hat{S}_{\mu\nu}(\mathbf{r}', t) \hat{S}_{\gamma\delta}(\mathbf{r}, t) \rangle &= \langle \hat{S}_{\alpha\beta}(\mathbf{r}'', t) \rangle \langle \hat{S}_{\mu\nu}(\mathbf{r}', t) \hat{S}_{\gamma\delta}(\mathbf{r}, t) \rangle + \langle \hat{S}_{\alpha\beta}(\mathbf{r}'', t) \hat{S}_{\mu\nu}(\mathbf{r}', t) \rangle \langle \hat{S}_{\gamma\delta}(\mathbf{r}, t) \rangle \\ &+ \langle \hat{S}_{\alpha\beta}(\mathbf{r}'', t) \hat{S}_{\gamma\delta}(\mathbf{r}, t) \rangle \langle \hat{S}_{\mu\nu}(\mathbf{r}', t) \rangle - 2 \langle \hat{S}_{\alpha\beta}(\mathbf{r}'', t) \rangle \langle \hat{S}_{\mu\nu}(\mathbf{r}', t) \rangle \langle \hat{S}_{\gamma\delta}(\mathbf{r}, t) \rangle. \end{aligned} \quad (\text{B8})$$

Under such consideration, the equations of motion for the one-body and two-body DM elements can be made to be closed, and they can be solved by using the above mentioned perturbation expansion [39,40].

a. Second-order solutions

At this order, the equations read

$$\begin{bmatrix} d_{31} & \Omega_c^* & 0 \\ \Omega_c & d_{41} + d_{31} & \Omega_c^* \\ 0 & 2\Omega_c & 2d_{41} - V \end{bmatrix} \begin{bmatrix} \rho_{31,31}^{(2)} \\ \rho_{41,31}^{(2)} \\ \rho_{41,41}^{(2)} \end{bmatrix} = \begin{bmatrix} -a_{31}^{(1)} \rho_{11}^{(0)} \\ -a_{41}^{(1)} \rho_{11}^{(0)} \\ 0 \end{bmatrix} \Omega_{p1}^2, \quad (\text{B9})$$

$$\begin{bmatrix} d_{32} & \Omega_c^* & 0 \\ \Omega_c & d_{32} + d_{42} & \Omega_c^* \\ 0 & 2\Omega_c & 2d_{42} - V \end{bmatrix} \begin{bmatrix} \rho_{32,32}^{(2)} \\ \rho_{42,32}^{(2)} \\ \rho_{42,42}^{(2)} \end{bmatrix} = \begin{bmatrix} -a_{32}^{(1)} \rho_{22}^{(0)} \\ -a_{42}^{(1)} \rho_{22}^{(0)} \\ 0 \end{bmatrix} \Omega_{p2}^2, \quad (\text{B10})$$

$$\begin{bmatrix} d_{41} + d_{42} - V & \Omega_c & \Omega_c & 0 \\ \Omega_c^* & d_{41} + d_{32} & 0 & \Omega_c \\ \Omega_c^* & 0 & d_{42} + d_{31} & \Omega_c \\ 0 & \Omega_c^* & \Omega_c^* & d_{32} + d_{31} \end{bmatrix} \begin{bmatrix} \rho_{42,41}^{(2)} \\ \rho_{41,32}^{(2)} \\ \rho_{42,31}^{(2)} \\ \rho_{32,31}^{(2)} \end{bmatrix} = \begin{bmatrix} 0 \\ -a_{41}^{(1)} \rho_{22}^{(0)} \\ -a_{42}^{(1)} \rho_{11}^{(0)} \\ -a_{32}^{(1)} \rho_{11}^{(0)} - a_{31}^{(1)} \rho_{22}^{(0)} \end{bmatrix} \Omega_{p1} \Omega_{p2}, \quad (\text{B11})$$

$$\begin{bmatrix} d_{42} + d_{14} & \Omega_c & -\Omega_c^* & 0 \\ \Omega_c^* & d_{32} + d_{14} & 0 & -\Omega_c^* \\ -\Omega_c & 0 & d_{42} + d_{13} & \Omega_c \\ 0 & -\Omega_c & \Omega_c^* & d_{32} + d_{13} \end{bmatrix} \begin{bmatrix} \rho_{42,14}^{(2)} \\ \rho_{32,14}^{(2)} \\ \rho_{42,13}^{(2)} \\ \rho_{32,13}^{(2)} \end{bmatrix} = \begin{bmatrix} 0 \\ -a_{14}^{(1)} \rho_{22}^{(0)} \\ a_{42}^{(1)} \rho_{11}^{(0)} \\ a_{32}^{(1)} \rho_{11}^{(0)} - a_{13}^{(1)} \rho_{22}^{(0)} \end{bmatrix} \Omega_{p1}^* \Omega_{p2}, \quad (\text{B12})$$

$$\begin{bmatrix} d_{41} + d_{14} & -\Omega_c^* & \Omega_c & 0 \\ -\Omega_c & d_{41} + d_{13} & 0 & \Omega_c \\ \Omega_c^* & 0 & d_{31} + d_{14} & -\Omega_c^* \\ 0 & \Omega_c^* & -\Omega_c & d_{31} + d_{13} \end{bmatrix} \begin{bmatrix} \rho_{41,14}^{(2)} \\ \rho_{41,13}^{(2)} \\ \rho_{31,14}^{(2)} \\ \rho_{31,13}^{(2)} \end{bmatrix} = \begin{bmatrix} 0 \\ a_{41}^{(1)} \rho_{11}^{(0)} \\ -a_{14}^{(1)} \rho_{11}^{(0)} \\ 2i\text{Im}(a_{31}^{(1)}) \rho_{11}^{(0)} \end{bmatrix} |\Omega_{p1}|^2, \quad (\text{B13})$$

$$\begin{bmatrix} d_{42} + d_{24} & -\Omega_c^* & \Omega_c & 0 \\ -\Omega_c & d_{42} + d_{23} & 0 & \Omega_c \\ \Omega_c^* & 0 & d_{32} + d_{24} & -\Omega_c \\ 0 & \Omega_c^* & -\Omega_c & d_{23} + d_{32} \end{bmatrix} \begin{bmatrix} \rho_{42,24}^{(2)} \\ \rho_{42,23}^{(2)} \\ \rho_{32,24}^{(2)} \\ \rho_{32,23}^{(2)} \end{bmatrix} = \begin{bmatrix} 0 \\ a_{42}^{(1)} \rho_{22}^{(0)} \\ -a_{24}^{(1)} \rho_{22}^{(0)} \\ 2i\text{Im}(a_{32}^{(1)}) \rho_{22}^{(0)} \end{bmatrix} |\Omega_{p2}|^2. \quad (\text{B14})$$

b. Third-order solutions

At this order, the number of equations are too many to be listed here. Here we present some of them for obtaining the solutions of $\rho_{44,41}^{(3)}$ and $\rho_{44,42}^{(3)}$, i.e.,

$$\begin{bmatrix} M_{11} & -\Omega_c^* & \Omega_c & \Omega_c & 0 & 0 & 0 & 0 \\ -\Omega_c & M_{12} & 0 & 0 & \Omega_c & \Omega_c & 0 & 0 \\ \Omega_c^* & 0 & M_{13} & 0 & -\Omega_c^* & 0 & \Omega_c & 0 \\ \Omega_c^* & 0 & 0 & M_{14} & 0 & -\Omega_c^* & \Omega_c & 0 \\ -i\Gamma_{34} & \Omega_c^* & -\Omega_c & 0 & M_{15} & 0 & 0 & \Omega_c \\ 0 & \Omega_c^* & 0 & -\Omega_c & 0 & M_{16} & 0 & \Omega_c \\ 0 & 0 & \Omega_c^* & \Omega_c^* & 0 & 0 & M_{17} & -\Omega_c^* \\ 0 & 0 & 0 & -i\Gamma_{34} & \Omega_c^* & \Omega_c^* & -\Omega_c & M_{18} \end{bmatrix} \begin{bmatrix} \rho_{44,41}^{(3)} \\ \rho_{43,41}^{(3)} \\ \rho_{41,34}^{(3)} \\ \rho_{44,31}^{(3)} \\ \rho_{41,33}^{(3)} \\ \rho_{43,31}^{(3)} \\ \rho_{34,31}^{(3)} \\ \rho_{33,31}^{(3)} \end{bmatrix} = \begin{bmatrix} R_{11} \\ R_{12} \\ R_{13} \\ R_{14} \\ R_{15} \\ R_{16} \\ R_{17} \\ R_{18} \end{bmatrix}, \quad (\text{B15})$$

where $M_{11} = i\Gamma_{34} + d_{41} - V$, $M_{12} = d_{43} + d_{41} - V$, $M_{13} = d_{34} + d_{41}$, $M_{14} = d_{31} + i\Gamma_{34}$, $M_{15} = i\Gamma_3 + d_{41}$, $M_{16} = d_{43} + d_{31}$, $M_{17} = d_{31} + d_{34}$, $M_{18} = d_{31} + i\Gamma_3$,

$$\begin{aligned} R_{11} &= 0, & R_{12} &= [a_{41,41}^{(2)}|\Omega_{p1}|^2 + a_{42,41}^{(2)}|\Omega_{p2}|^2]\Omega_{p1}, \\ R_{13} &= [-a_{41,14}^{(2)}|\Omega_{p1}|^2 - a_{41,24}^{(2)}|\Omega_{p2}|^2]\Omega_{p1}, \\ R_{14} &= [-a_{44,1}^{(2)}\rho_{11}^{(0)}|\Omega_{p1}|^2 - a_{44,2}^{(2)}\rho_{11}^{(0)}|\Omega_{p2}|^2]\Omega_{p1}, \\ R_{15} &= [(a_{41,31}^{(2)} - a_{41,13}^{(2)})|\Omega_{p1}|^2 + (a_{41,32}^{(2)} - a_{41,23}^{(2)})|\Omega_{p2}|^2]\Omega_{p1}, \\ R_{16} &= [(a_{41,31}^{(2)} - a_{43,1}^{(2)}\rho_{11}^{(0)})|\Omega_{p1}|^2 + (a_{42,31}^{(2)} - a_{43,2}^{(2)}\rho_{11}^{(0)})|\Omega_{p2}|^2]\Omega_{p1}, \\ R_{17} &= [-(a_{31,14}^{(2)} + a_{34,1}^{(2)}\rho_{11}^{(0)})|\Omega_{p1}|^2 - (a_{31,24}^{(2)} + a_{34,2}^{(2)}\rho_{11}^{(0)})|\Omega_{p2}|^2]\Omega_{p1}, \\ R_{18} &= (a_{31,31}^{(2)} - a_{31,13}^{(2)} - a_{33,1}^{(2)}\rho_{11}^{(0)})|\Omega_{p1}|^2\Omega_{p1} + (a_{32,31}^{(2)} - a_{31,23}^{(2)} - a_{33,2}^{(2)}\rho_{11}^{(0)})|\Omega_{p2}|^2\Omega_{p1}, \end{aligned}$$

and

$$\begin{bmatrix} M_{21} & -\Omega_c^* & \Omega_c & \Omega_c & 0 & 0 & 0 & 0 \\ -\Omega_c & M_{22} & 0 & 0 & \Omega_c & \Omega_c & 0 & 0 \\ \Omega_c^* & 0 & M_{23} & 0 & -\Omega_c^* & 0 & \Omega_c & 0 \\ \Omega_c^* & 0 & 0 & M_{24} & 0 & -\Omega_c^* & \Omega_c & 0 \\ -i\Gamma_{34} & \Omega_c^* & -\Omega_c & 0 & M_{25} & 0 & 0 & \Omega_c \\ 0 & \Omega_c^* & 0 & -\Omega_c & 0 & M_{26} & 0 & \Omega_c \\ 0 & 0 & \Omega_c^* & \Omega_c^* & 0 & 0 & M_{27} & -\Omega_c^* \\ 0 & 0 & 0 & -i\Gamma_{34} & \Omega_c^* & \Omega_c^* & -\Omega_c & M_{28} \end{bmatrix} \begin{bmatrix} \rho_{44,42}^{(3)} \\ \rho_{43,42}^{(3)} \\ \rho_{42,34}^{(3)} \\ \rho_{44,32}^{(3)} \\ \rho_{42,33}^{(3)} \\ \rho_{43,32}^{(3)} \\ \rho_{34,32}^{(3)} \\ \rho_{33,32}^{(3)} \end{bmatrix} = \begin{bmatrix} R_{21} \\ R_{22} \\ R_{23} \\ R_{24} \\ R_{25} \\ R_{26} \\ R_{27} \\ R_{28} \end{bmatrix}, \quad (\text{B16})$$

where $M_{21} = d_{42} + i\Gamma_{34} - V$, $M_{22} = d_{43} + d_{42} - V$, $M_{23} = d_{34} + d_{42}$, $M_{24} = d_{32} + i\Gamma_{34}$, $M_{25} = d_{42} + i\Gamma_3$, $M_{26} = d_{43} + d_{32}$, $M_{27} = d_{34} + d_{32}$, $M_{28} = d_{32} + i\Gamma_3$,

$$\begin{aligned} R_{21} &= 0, & R_{22} &= [a_{42,41}^{(2)}|\Omega_{p1}|^2 + a_{42,42}^{(2)}|\Omega_{p2}|^2]\Omega_{p2}, \\ R_{23} &= [-a_{42,14}^{(2)}|\Omega_{p2}|^2 - a_{42,24}^{(2)}|\Omega_{p2}|^2]\Omega_{p2}, \\ R_{24} &= [-a_{44,1}^{(2)}\rho_{22}^{(0)}|\Omega_{p1}|^2 - a_{44,2}^{(2)}\rho_{22}^{(0)}|\Omega_{p2}|^2]\Omega_{p2}, \\ R_{25} &= [(a_{42,31}^{(2)} - a_{42,13}^{(2)})|\Omega_{p1}|^2 + (a_{42,32}^{(2)} - a_{42,23}^{(2)})|\Omega_{p2}|^2]\Omega_{p2}, \\ R_{26} &= [(a_{41,32}^{(2)} - a_{43,1}^{(2)}\rho_{22}^{(0)})|\Omega_{p1}|^2 + (a_{42,32}^{(2)} - a_{43,2}^{(2)}\rho_{22}^{(0)})|\Omega_{p2}|^2]\Omega_{p2}, \\ R_{27} &= [-(a_{32,14}^{(2)} + a_{34,1}^{(2)}\rho_{22}^{(0)})|\Omega_{p1}|^2 - (a_{32,24}^{(2)} + a_{34,2}^{(2)}\rho_{22}^{(0)})|\Omega_{p2}|^2]\Omega_{p2}, \\ R_{28} &= [(a_{32,31}^{(2)} - a_{32,13}^{(2)} - a_{33,1}^{(2)}\rho_{22}^{(0)})|\Omega_{p1}|^2 + (a_{32,32}^{(2)} - a_{32,23}^{(2)} - a_{33,2}^{(2)}\rho_{22}^{(0)})|\Omega_{p2}|^2]\Omega_{p2}. \end{aligned}$$

Solving the above two equations, we obtain

$$\rho_{44,41}^{(3)} = a_{44,41,1}^{(3)}|\Omega_{p1}|^2\Omega_{p1} + a_{44,41,2}^{(3)}|\Omega_{p2}|^2\Omega_{p1}, \quad (\text{B17a})$$

$$\rho_{44,42}^{(3)} = a_{44,42,1}^{(3)}|\Omega_{p1}|^2\Omega_{p2} + a_{44,42,2}^{(3)}|\Omega_{p2}|^2\Omega_{p2}, \quad (\text{B17b})$$

with

$$a_{44,4j,l}^{(3)} = \frac{P_{j10} + P_{j11}V(\mathbf{r}' - \mathbf{r}) + P_{j12}V(\mathbf{r}' - \mathbf{r})^2}{Q_{j10} + Q_{j11}V(\mathbf{r}' - \mathbf{r}) + Q_{j12}V(\mathbf{r}' - \mathbf{r})^2 + Q_{j13}V(\mathbf{r}' - \mathbf{r})^3}, \quad (\text{B18})$$

where P_{jln} and Q_{jln} ($j, l = 1, 2; n = 0, 1, 2, 3$) are constants, depending on the spontaneous emission and dephasing rates, detunings, half Rabi frequency of the control field, and other system parameters. The explicit expressions of P_{jln} and Q_{jln} are very lengthy and hence are omitted here.

With the above solutions, we obtain the nonlinear coupled equations for the motion of Ω_{p1} and Ω_{p2} up to the third-order approximation. They are given by

$$\begin{aligned} i\frac{\partial}{\partial z_2}\Omega_{p1} + \frac{c}{2\omega_{p1}}\nabla_{\perp}^2\Omega_{p1} + \kappa_{13}(a_{31,1}^{(3)}|\Omega_{p1}|^2 + a_{31,2}^{(3)}|\Omega_{p2}|^2)\Omega_{p1} \\ + \kappa_{13}\mathcal{N}_a \int d^3r' a_{31,3}^{(3)}V(\mathbf{r}' - \mathbf{r})|\Omega_{p1}(\mathbf{r}')|^2\Omega_{p1}(\mathbf{r}) + \kappa_{13}\mathcal{N}_a \int d^3r' a_{31,4}^{(3)}V(\mathbf{r}' - \mathbf{r})|\Omega_{p2}(\mathbf{r}')|^2\Omega_{p1}(\mathbf{r}) = 0, \end{aligned} \quad (\text{B19a})$$

$$i \frac{\partial}{\partial z_2} \Omega_{p2} + \frac{c}{2\omega_{p2}} \nabla_{\perp}^2 \Omega_{p2} + \kappa_{23} (a_{32,1}^{(3)} |\Omega_{p1}|^2 + a_{32,2}^{(3)} |\Omega_{p2}|^2) \Omega_{p2} \\ + \kappa_{23} \mathcal{N}_a \int d^3 r' a_{32,3}^{(3)} V(\mathbf{r}' - \mathbf{r}) |\Omega_{p1}(\mathbf{r}')|^2 \Omega_{p2}(\mathbf{r}) + \kappa_{23} \mathcal{N}_a \int d^3 r' a_{32,4}^{(3)} V(\mathbf{r}' - \mathbf{r}) |\Omega_{p2}(\mathbf{r}')|^2 \Omega_{p2}(\mathbf{r}) = 0. \quad (\text{B19b})$$

Equations (4a) and (4b) in the main text can be readily obtained from the above nonlinear coupled equations.

-
- [1] L. Rayleigh, LVI. Investigations in optics, with special reference to the spectroscope, *Philos. Mag.* **8**, 261 (1879).
- [2] M. Born and E. Wolf, *Principles of Optics*, 6th ed. (Pergamon, New York, 1980).
- [3] R. R. Moseley, S. Shepherd, D. J. Fulton, B. D. Sinclair, and M. H. Dunn, Spatial Consequences of Electromagnetically Induced Transparency: Observation of Electromagnetically Induced Focusing, *Phys. Rev. Lett.* **74**, 670 (1995).
- [4] R. R. Moseley, S. Shepherd, D. J. Fulton, B. D. Sinclair, and M. H. Dunn, Electromagnetically-induced focusing, *Phys. Rev. A* **53**, 408 (1996).
- [5] A. G. Truscott, M. E. J. Friese, N. R. Heckenberg, and H. Rubinsztein-Dunlop, Optically Written Waveguide in An Atomic Vapor, *Phys. Rev. Lett.* **82**, 1438 (1999).
- [6] R. Kapoor and G. S. Agarwal, Theory of electromagnetically induced waveguides, *Phys. Rev. A* **61**, 053818 (2000).
- [7] D. D. Yavuz and N. A. Proite, Nanoscale resolution fluorescence microscopy using electromagnetically induced transparency, *Phys. Rev. A* **76**, 041802(R) (2007).
- [8] A. V. Gorshkov, L. Jiang, M. Greiner, P. Zoller, and M. D. Lukin, Coherent Quantum Optical Control with Subwavelength Resolution, *Phys. Rev. Lett.* **100**, 093005 (2008).
- [9] O. Firstenberg, M. Shuker, N. Davidson, and A. Ron, Elimination of the Diffraction of Arbitrary Images Imprinted on Slow Light, *Phys. Rev. Lett.* **102**, 043601 (2009).
- [10] O. Firstenberg, P. London, M. Shuker, A. Ron, and N. Davidson, Elimination, reversal and directional bias of optical diffraction, *Nat. Phys.* **5**, 665 (2009).
- [11] G. Vemuri, G. S. Agarwal, and K. V. Vasavada, Cloning, Dragging, and Parametric Amplification of Solitons in a Coherently Driven, Nonabsorbing System, *Phys. Rev. Lett.* **79**, 3889 (1997).
- [12] M. Kiffner, J. Evers, and M. S. Zubairy, Resonant Interferometric Lithography beyond the Diffraction Limit, *Phys. Rev. Lett.* **100**, 073602 (2008).
- [13] P. K. Vudyaasetu, D. J. Starling, and J. C. Howell, All Optical Waveguiding in a Coherent Atomic Rubidium Vapor, *Phys. Rev. Lett.* **102**, 123602 (2009).
- [14] K. T. Kapale and G. S. Agarwal, Sub-nanoscale resolution for microscopy via coherent population trapping, *Opt. Lett.* **35**, 2792 (2010).
- [15] T. N. Dey and J. Evers, Nondiffracting optical beams in a three-level Raman system, *Phys. Rev. A* **84**, 043842 (2011).
- [16] O. Verma, L. Zhang, J. Evers, and T. Dey, Optical cloning of arbitrary images beyond the diffraction limits, *Phys. Rev. A* **88**, 013810 (2013).
- [17] D.-S. Ding, Z.-Y. Zhou, and B.-S. Shi, Image cloning beyond diffraction based on coherent population trapping in a hot rubidium vapor, *Opt. Lett.* **39**, 240 (2014).
- [18] M. Cao, L. Zhang, Y. Yu, F. Ye, D. Wei, W. Guo, S. Zhang, H. Cao, and F. Li, Transfer and conversion of images based on EIT in atom vapor, *Opt. Lett.* **39**, 2723 (2014).
- [19] T. N. Dey and G. S. Agarwal, Sub-diffraction propagation of images using saturated absorption of optical transition, *Opt. Lett.* **34**, 3199 (2009).
- [20] O. Verma and T. Dey, Steering, splitting, and cloning of an optical beam in a coherently driven Raman gain system, *Phys. Rev. A* **91**, 013820 (2015).
- [21] U. F. Apolinario, S. Manzoor, and L. E. E. De Araujo, Optical image cloning based on electromagnetic induced absorption, *Opt. Lett.* **42**, 4966 (2017).
- [22] J. A. Andersen, M. E. J. Friese, A. G. Truscott, Z. Ficek, P. D. Drummond, N. R. Heckenberg, and H. Rubinsztein-Dunlop, Light guiding light: Nonlinear refraction in rubidium vapor, *Phys. Rev. A* **63**, 023820 (2001).
- [23] M. Vengalattore and M. Prentiss, Radial Confinement of Light in An Ultracold Anisotropic Medium, *Phys. Rev. Lett.* **95**, 243601 (2005).
- [24] D. Bortman-Arbiv, A. D. Wilson-Gordon, and H. Friedmann, Strong parametric amplification by spatial soliton-induced cloning of transverse beam profiles in an all-optical anti-waveguide, *Phys. Rev. A* **63**, 031801(R) (2001).
- [25] T. F. Gallagher, *Rydberg Atoms* (Cambridge University, Cambridge, England, 2008).
- [26] M. Saffman, T. G. Walker, and K. Mølmer, Quantum information with Rydberg atoms, *Rev. Mod. Phys.* **82**, 2313 (2010).
- [27] J. Sinclair, D. Angulo, N. Lupu-Gladstein, K. Bonsma-Fisher, and A. M. Steinberg, Observation of a large, resonant, cross-Kerr nonlinearity in a cold Rydberg gas, *Phys. Rev. Research* **1**, 033193 (2019).
- [28] S. Sevinçli, N. Henkel, C. Ates, and T. Pohl, Nonlocal Nonlinear Optics in Cold Rydberg Gases, *Phys. Rev. Lett.* **107**, 153001 (2011).
- [29] J. D. Pritchard, K. J. Weatherill, and C. S. Adams, Nonlinear optics using cold Rydberg atoms, *Annu. Rev. Cold At. Mol.* **1**, 301 (2013).
- [30] W. Li, D. Viscor, S. Hofferberth, and I. Lesanovsky, Electromagnetically Induced Transparency in An Entangled Medium, *Phys. Rev. Lett.* **112**, 243601 (2014).
- [31] O. Firstenberg, C. S. Adams, and S. Hofferberth, Nonlinear quantum optics mediated by Rydberg interactions, *J. Phys. B* **49**, 152003 (2016).
- [32] C. Murray and T. Pohl, Quantum and nonlinear optics in strongly interacting atomic ensembles, in *Advances in Atomic, Molecular, and Optical Physics*, Vol. 65 (Academic, New York, 2016), Chap. 7, pp. 321–372.
- [33] E. Lantz, Medical imaging: Retracing random paths, *Nat. Photonics* **2**, 71 (2008).

- [34] B. E. Cohen, Biological imaging: Beyond fluorescence, *Nature (London)* **467**, 407 (2010).
- [35] For simplicity, we assume the Rydberg state $|4\rangle$ is a S state, so the interaction between the Rydberg atoms is isotropic.
- [36] In our model, the j th probe laser field has the energy flux density $S_j = \epsilon_0 c n_{pj} (2\hbar/|\mathbf{p}_{j3}|)^2 |\Omega_{pj}|^2$, where $n_{pj} \approx 1 + \chi_j^{(1)}/2 \approx 1$ is the refractive index. With the parameters used in our paper, we have $S_1 \approx S_2 = 2.46 \times 10^{-2}$ W/cm². Thus the photon number per second per square micrometer is given by $S_j/E_{\text{photon}} = 5.68 \times 10^8$, where $E_{\text{photon}} \approx 4.3 \times 10^{-19}$ J is the photon energy of the probe fields ($E_{\text{photon}} = \hbar\omega_{p1} \approx \hbar\omega_{p2}$). Because the atoms we are considering interact resonantly with the probe fields, the atomic absorption cross-section $\sigma \approx \lambda_{pj}^2$ (where $\lambda_{p1} \approx \lambda_{p2} = 0.461$ μm). Thus the photon number per second per atomic absorption cross-section is $(0.461)^2 \times 5.68 \times 10^8 = 1.21 \times 10^8$. This tells us that a semiclassical approach can be employed safely for our system.
- [37] Z. Chen and G. Huang, Trapping of weak signal pulses by soliton and trajectory control in a coherent atomic gas, *Phys. Rev. A* **89**, 033817 (2014).
- [38] A. C. Newell and J. V. Moloney, *Nonlinear Optics* (Addison-Wesley, Reading, MA, 1990).
- [39] Z. Bai and G. Huang, Enhanced third-order and fifth-order Kerr nonlinearities in a cold atomic system via atom-atom interaction, *Opt. Express* **24**, 4442 (2016).
- [40] Z. Bai, W. Li, and G. Huang, Stable single light bullets and vortices and their active control in cold Rydberg gases, *Optica* **6**, 309 (2019).
- [41] S. Mauger, J. Millen, and M. P. A. Jones, Spectroscopy of strontium Rydberg states using electromagnetically induced transparency, *J. Phys. B* **40**, F319 (2007).
- [42] R. Mukherjee, J. Millen, R. Nath, M. P. A. Jones, and T. Pohl, Many-body physics with alkaline-earth Rydberg lattices, *J. Phys. B* **44**, 184010 (2011).
- [43] F. B. Dunning, T. C. Killian, S. Yoshida, and J. Burgdörfer, Recent advances in Rydberg physics using alkaline-earth atoms, *J. Phys. B* **49**, 112003 (2016).
- [44] F. Robicheaux, Calculations of long range interactions for ⁸⁷Sr Rydberg states, *J. Phys. B* **52**, 244001 (2019).
- [45] To realize the optical cloning, the system is required to possess self-focused Kerr nonlinearity (i.e., the dispersion parameter C_6 must be positive) and support the double Rydberg-EIT. For most alkali-metal atoms, C_6 is negative and thus does not allow self-focused Kerr nonlinearity. Alkaline-earth atoms ⁸⁸Sr have positive C_6 , but their ground state has no fine and hyperfine structures (quantum number of orbital angular momentum $L = 0$, quantum number of nuclear spin $I = 0$) and hence it is not possible to realize the double Rydberg-EIT. However, the alkaline-earth atoms ⁸⁷Sr may have positive C_6 [44] and have a hyperfine structure for the ground state ($L = 0$, $I = 9/2$). Consequently, the ⁸⁷Sr atomic gas is a possible candidate for realizing the self-focused Kerr nonlinearity and thus the double Rydberg-EIT and optical cloning suggested in the present paper.
- [46] Here $\langle \hat{S}_{\alpha\beta} \rangle = \langle \Psi(0) | \hat{S}_{\alpha\beta} | \Psi(0) \rangle$, with $|\Psi(0)\rangle$ the initial quantum state of the atomic gas where all the atoms are populated in the ground state $|1\rangle$ and $|2\rangle$ before the two probe laser fields are applied.
- [47] For simplicity, in the numerical calculations carried out in this paper we shall assume the initial DM elements of the atoms to be $\rho_{11}^{(0)} \approx \rho_{22}^{(0)} = 0.5$ (other $\rho_{\alpha\beta}^{(0)} = 0$).
- [48] S. Mukamel, *Principles of Nonlinear Optical Spectroscopy* (Oxford University, London, 1995).